Intersubband resonant effects of dissipative transport in quantum wires

D. Jovanovic, S. Briggs, and J. P. Leburton
Beckman Institute for Advanced Science and Technology and the Department of Electrical and Computer Engineering, University of Illinois at Urbana-Champaign, Urbana, Illinois 61801
(Received 3 May 1990)

We investigate the effects of inelastic optical- and acoustic-phonon scattering in quasi-one-dimensional systems with up to 20 subbands. We use a direct-integration Monte Carlo method to study intersubband scattering effects when the subband spacing approaches resonance ($n\Delta E$ being the optical-phonon energy of 36 meV). Simulations performed on first-, second-, and third-order resonant structures at temperatures ranging from 150 to 300 K reveal the appearance of dissipative transport properties. Specifically, nonlinearities in the electron distribution induce velocity fluctuations analogous to the longitudinal magnetophonon effect and generate population inversions between adjacent subbands.

INTRODUCTION

Contemporary confinement capabilities are approaching the point where subband-dependent phenomena are experimentally realizable in quasi-one-dimensional (1D) systems.[1-4] Ismail *et al.*[5] recently reported on the observation of Shubnikov–de Haas–type oscillations in the longitudinal resistance of electrostatically confined 1D systems. This observation is important for two reasons. It shows that, despite inherent irregularities in the fabrication of a set of 100 parallel quantum wires, fluctuations in the confining potential are not a cause of significant quantum-effect smearing, and, second, oscillations persist at temperatures as high as 77 K. Physically, the presence of subbands in low-dimensional systems is a quantum-mechanical consequence of transverse confinement and can be expected to introduce subband-dependent effects in dissipative transport processes.[6,7] These effects can become quite significant as the degree of confinement increases with improved technological resolutions. Specifically, when the intersubband spacing approaches kT at room temperature, novel quantum transport[8] and optical[9] properties are expected to occur.

The purpose of this investigation is to discuss the effects of resonant intersubband optical-phonon scattering[10] (RISOPS) in 1D systems. Two subbands are defined to be in resonance when the energy spacing between them approaches the polar optical-phonon (POP) energy ($\hbar\omega_{\rm LO}=36$ meV for GaAs). Of specific interest are high-order resonances for which one or more nonresonant subbands lie between the two bands in resonance. Such structures are found to generate transport phenomena up to the third order configuration. As the spectrum of 1D subbands is passed through resonance, a velocity minimum similar to the longitudinal magnetophonon (LMP) effect occurs at both 150 and 300 K. For device applications, such an effect carries the potential for negative differential resistance. In addition, the resonant configuration is found to maintain a population inversion between the resonant subband and a lower adjacent subband. To investigate these phenomena, we perform single-carrier multisubband Monte Carlo simulations of an idealized GaAs-$Al_xGa_{1-x}As$ 1D structure. Inelastic polar optical and acoustic[11] phonons are taken as the dominant scattering mechanisms to enable simulations from 150 K to room temperature. Appropriate broadening of the 1D density of states is included to account for quantum effects in the electron-phonon interaction. Low confinement structures are simulated by allowing up to 20 subbands to be modeled at once. This is accomplished primarily by employing a recursive algorithm for computing harmonic-oscillator matrix elements and a novel "on-line" method for updating phase-space information in the Monte Carlo code.

MODEL

We model transverse confinement via an infinite square-well approximation to a heterojunction quantum well and an electrostatic harmonic-oscillator potential. Although experimentally unrealistic, the square-well potential does not seriously affect the accuracy of our model since it is the energy eigenspectrum rather than the nature of the wave functions that determines the overall behavior of quasi-1D systems. By considering only weak harmonic-oscillator potentials, the nature of the eigenspectrum is dominated by harmonic-oscillator eigenenergies and the influence of the highly confined square-well potential is minimized. Furthermore, the inclusion of the square-well potential, as opposed to a more realistic electrostatic quasitriangular potential, introduces a significant degree of computational simplicity into our code.

Both of our potential profiles are distributed over many lattice constants, thereby allowing use of the effective-mass approximation. The simulated energy space extends 400 meV above the Γ-valley bottom since we assume that electrons occupy 3D states above this limit. A similar model[12] incorporating nonparabolicity and intervalley scattering demonstrates the validity of our approximations for small longitudinal fields ($F_x \leq 500$ V/cm). Although important for studying the effects of disorder

and localization, impurity scattering is neglected in the present simulation since these types of scattering events are rare in modulation-doped GaAs structures.[13,14] The above approximations are primarily invoked to ease the computational requirements involved with simulating systems with up to 20 subbands. Wave functions for the transverse dimensions are solved analytically and the intersubband scattering rates are subsequently computed in the Born approximation. The quantum-well wave function reads

$$\psi(z)=\left[\frac{2}{L_z}\right]^{1/2}\sin\left[\frac{\pi z}{L_z}\right], \tag{1}$$

where L_z represents the width of the well. The quantum number has been purposely omitted since we consider only one quantum-well state throughout our simulation. Intersubband scattering then occurs between harmonic-oscillator levels with analytical wave functions given by

$$\phi_n(y)=\left[\frac{m^*\omega}{\pi\hbar(n!)^2}\right]^{1/4}H_n(\xi)e^{-\xi^2/4}, \tag{2}$$

where

$$\xi=(2m^*\omega/\hbar)^{1/2}y . \tag{3}$$

Here, ω is the proper frequency of the harmonic oscillator and n is the index of the quantum state. Electron transport is driven in the x direction by a longitudinally applied field, F_x, which gives rise to a weak field-dependent Airy-potential spectrum. By restricting our simulations to low fields, quantum effects arising from F_x are negligible and free-electron wave functions within the effective-mass approximation suitably describe electron transport. Therefore, the spectrum of subband energies is given by

$$E_n(k_x)=\frac{\pi^2\hbar^2}{2m^*L_x^2}+\hbar\omega(n+1/2)+\frac{\hbar^2k_x^2}{2m^*}, \tag{4}$$

where k_x is the longitudinal wave vector. Again, note that the index corresponding to the quantum-well eigenspectrum is explicitly omitted since only one subband is considered for this potential. From these wave functions and energy spectra, intersubband transition probabilities are computed for the inelastic POP interaction using the Fröhlich polaron formalism,[15] and for acoustic phonons via deformation-potential scattering. Recent investigation[16] on phonon dispersion in confined systems indicates that optic modes can be significantly quantized in quasi-1D structures. However, as we are interested in the first-order effects of transport processes, we neglect the particular influence of phonon confinement and restrict our study to bulk modes. Using Fermi's golden rule, the transition probabilities are given by

$$S(\mathbf{k},\mathbf{k}')=\frac{2\pi}{\hbar}|M_{nn'}(\mathbf{k},\mathbf{k}')|^2\delta(E(\mathbf{k}')-E(\mathbf{k})\pm\hbar\omega_{\mathbf{q}}) . \tag{5}$$

Here, $\mathbf{k}$ and $\mathbf{k}'$ represent the initial and final wave vectors and n and n' represent initial and final subbands, respectively. The 1D matrix elements, $M_{nn'}(\mathbf{k},\mathbf{k}')$, can be rewritten with a variable transformation as

$$M_{nn'}(\mathbf{q})=V_q\delta_{k_x-k_x',\pm q_x}F(q_z)G_{nn'}(q_y) , \tag{6}$$

where

$$F(q_z)=\frac{\pi^2}{\pi^2-(q_zL_z/2)^2}\frac{\sin(q_zL_z/2)}{q_zL_z/2}e^{\pm iq_zL_x/2} , \tag{7}$$

$$G_{nn'}(q_y)=\int dy\,\phi_{n'}^*(y)\phi_n(y)e^{\pm iq_yy} , \tag{8}$$

and V_q is a coupling constant dependent on the type of interaction. The $\pm$ in the above equations indicate phonon absorption $(-)$ and emission $(+)$. Total scattering rates for each subband are then computed by summing over the final states giving

$$\frac{1}{\tau_n(E)}=\frac{V_{ol}}{\hbar(2\pi)^2}\sum_{n'}\int d\mathbf{q}|M_{nn'}(\mathbf{q})|^2 \times\delta(E(\mathbf{k}')-E(\mathbf{k})\pm\hbar\omega_{\mathbf{q}}) . \tag{9}$$

Of particular importance in simulating 1D multisubband systems at high temperatures is the issue of collision broadening. Specifically, the broadening of the phonon energy, $\delta E_{\rm ph}$, is a strong impediment to the observation of quantum effects at room temperature. A thorough treatment would tackle this problem by self-consistently[17] computing the polaron self-energy. Calculations of $\mathrm{Im}\Sigma$ for a single subband, however, indicate that scattering rates computed with a prebroadening 1D density of states give a good estimate to those obtained by the self-energy method.[18] We compute these prebroadened densities of states by convolving their exact form with a Gaussian distribution and taking $\delta E_{\rm ph}=2.3$ meV at 300 K and $\delta E_{\rm ph}=1.6$ meV at 150 K.

The computation of the 1D matrix elements presents the major bottleneck in our simulations. This step involves computing a table of the 1D matrix elements as functions of q_x. These are obtained numerically by a routine that performs a double integral of Eq. (6) over q_z and q_y. The input to this routine is a table of relevant values for q_x that are varied over 3 orders of magnitude ($7\times10^4\le q_x\le1.5\times10^7$ cm^{-1}) for acoustic phonons and 7 orders of magnitude ($1\times10^0\le q_x\le1\times10^7$ cm^{-1}) for polar optical phonons. Limits on q_x arise because below 7×10^4 cm^{-1}, the acoustic-phonon-dispersion relation is essentially independent of q_x while 1.5×10^7 cm^{-1} represents the maximum electron momentum limited by our energy space. A 20-subband system requires 420 such double integrations to fully model the effects of intersubband scattering. The computational overhead associated with these double integrations is greatly alleviated by the choice of a harmonic-oscillator confining potential that permits an efficient algorithm for computing the harmonic matrix elements, $G_{nn'}(q_y)$. Specifically, we generate Hermite polynomials recursively via

$$H_{n+1}(\xi)=\xi H_n(\xi)-nH_{n-1}(\xi) \tag{10}$$

thereby introducing appreciable vectorizability into our code. Using this technique, we obtain a speedup of 30% over the nonvectorized code when run on a CRAY-2. Also, storage of the 2D matrix elements is facilitated by

the reversibility of phonon emission and absorption processes between subbands [i.e., $M_{nn'}(\mathbf{k},\mathbf{k}')=M_{n'n}(\mathbf{k}',\mathbf{k})$]. The table of 1D matrix elements is then used as an input file to a routine that computes the total scattering rates in the manner specified by Eq. (9). The energy range for $1/\tau_n(E)$ varies from 0 to 400 meV and is divided into 2400 intervals. Due to memory limitations, the final-state information is suppressed at this stage and recomputed later in the Monte Carlo code. The total 1D scattering rates for a 20-subband second-order resonant system are shown in Fig. 1. Each line in Figs. 1(a) and 1(b) represents the total scattering rate for a particular subband, including both intrasubband and intersubband scattering processes, with the inset in Fig. 1(a) detailing the total rate (solid) for the first subband along with a decomposition into phonon emission (dash) and absorption (dash-dot) rates. All the rates show the characteristic peaking due to the 1D density of states with the large and smaller peaks corresponding to intrasubband POP emission and absorption, respectively. Secondary peaks that are smaller in magnitude occur at energies where intersubband transitions become possible. The effect of acoustic-phonon scattering is not noticeable due to the relatively weak coupling of the deformation-potential interaction. Differences between the rates at 300 and 150 K are accounted for by the phonon occupation number and broadening. Since both of these parameters decrease with temperature, the scattering rates at 300 K display broader peaks and a higher overall rate. Figure 1(b) shows that both phonon emission and absorption processes are still favorable at 150 K, despite the lower phonon occupation. This fact, coupled with the smaller broadening, implies that the effects of intersubband scattering will be more resolved at the lower temperature.

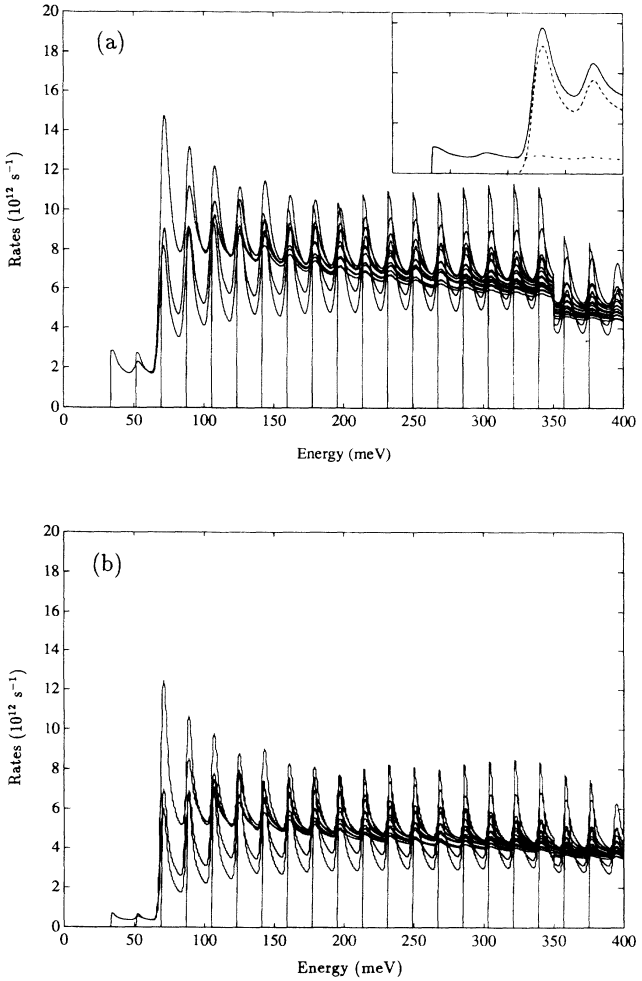

FIG. 1. (a) Total scattering rates for a 20-subband 1D system with $L_y=150$ Å and a second-order resonant harmonic-oscillator energy spectrum ($\hbar\omega=18$ meV). The rates are computed for $T=300$ K with a broadening energy $\delta E_{\rm ph}=2.3$ meV. The inset shows the emission (dashed) and absorption (dot-dashed) rates along with the total rate for the first subband. Intrasubband POP emission becomes dominant for energies $\hbar\omega_{\rm LO}$ above the subband bottom when final scattering states become available. (b) Total scattering rates for the same confinement as (a) but with $T=150$ K and $\delta E_{\rm ph}=1.6$ meV. In both figures the origin of the energy scale is taken as the Γ-valley bottom.

MONTE CARLO METHOD

Once a table of scattering rates is obtained, a direct integration Monte Carlo solution to the Boltzmann equation is used to track electronic motion under the influence of F_x. In the direct integration method, the probability that an electron in subband n, which suffered a collision at time $t=0$, scatters at time t is given by

$$-\ln(r)=\sum_{E=E_i}^{E_f}\frac{1}{\tau_n(E)}\Delta t(E)\ , \tag{11}$$

where r is a random number chosen from a uniform distribution. At invocation, the Monte Carlo program requests the longitudinal electric field, F_x, and an initial state for the electron. The electron is placed in the initial state and allowed to undergo 6000 scattering events to allow independence of its initial conditions. Statistics are collected for the next 1 000 000 scattering events to guarantee that the electron achieves steady-state conditions. After each free flight, a bin for the final wave vector, k_x', is updated and the electron is allowed to scatter by randomly choosing a scattering agent (acoustic or polar optic phonon). The final-state information is then computed for the chosen scattering process, a new initial wave vector is randomly chosen, and the electron is subsequently launched on another free flight. The computation of final-state information "on line" after each free flight is a departure from other multisubband Monte Carlo methods. This is necessary to accommodate the extensive memory requirements associated with simulating 20 subbands. Storing all the scattering-rate information in memory, as in the method proposed by Briggs *et al.*,[8] would require 30 Mb in our simulation. By storing only the total rates, we reduce the memory utilization to 500 Kb at the expense of making 80 relatively simple computations after each scattering event. What makes Monte Carlo simulations of quasi-1D devices particularly affordable is the restricted phase space found in 1D sys-

tems. Since the outcome of a scattering event can be forward emission, forward absorption, backward emission, or backward absorption, and since there are only two possible wave vectors corresponding to each energy, all possible values of $\Delta t(E)$ can be stored in a lookup table. This results in a significant speeding up of the integration over 2D and bulk simulations. The statistics generated by the Monte Carlo code are tables of before-scattering carrier concentrations, $n_{b,n}(E)$ are then obtained via[19]

$$f_n(E)=\frac{1}{g_{1D}(E)}\frac{\tau_n(E)}{\tau_0}n_{b,n}(E)\ , \tag{12}$$

where $g_{1D}(E)$ is the 1D density of states and τ_0 is an appropriate normalization constant that preserves the relative carrier concentrations over the entire set of subbands. A typical set of distribution functions is shown in Fig. 2 for the same confinement conditions as in Fig. 1. Carrier velocities and other properties of interest are obtained by averaging over the distribution functions for each subband.

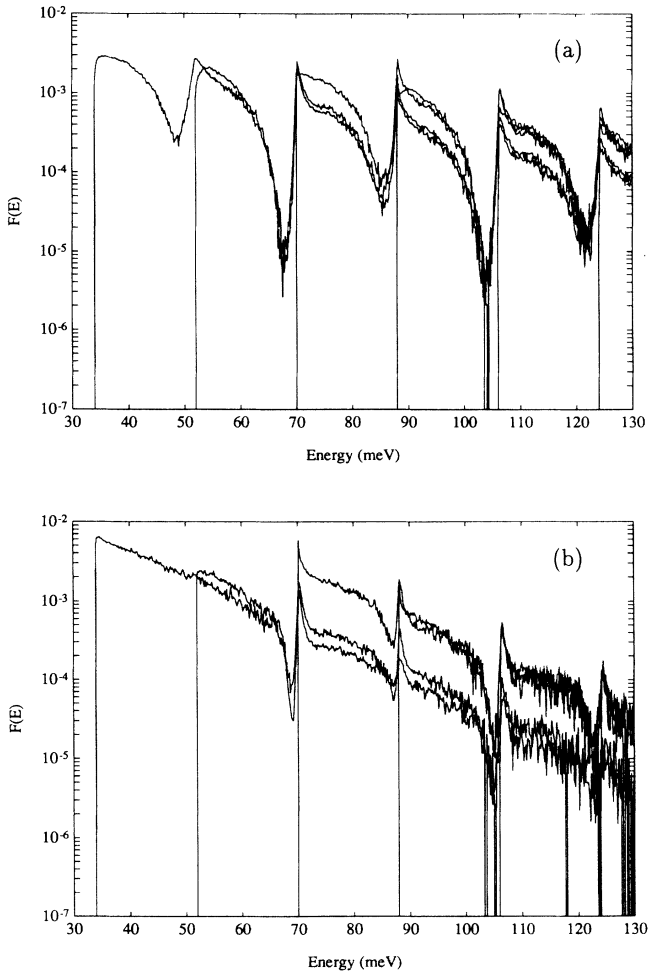

FIG. 2. Distribution functions for the second-order resonant system with $F_x=50$ V/cm at $T=300$ K and (b) $T=150$ K. Each curve represents the relative distribution function in a particular subband with the energy origin lying at the Γ-valley minimum. For clarity, only the first six subbands are shown.

RESULTS

We apply our simulation to study the effects of RISOPS on low field transport at 150 and 300 K, where the former temperature represents near optimal conditions for observing velocity oscillations analogous to the longitudinal magnetophonon (LMP) effect.[20,21] In general, low field distribution functions at 300 K show a high degree of nonlinearity just below the POP emission threshold as indicated in Fig. 2(a). This is attributed to the sharp peaking in the scattering rates for both absorption and emission, and the absence of angular randomization in 1D systems, both of which lead to depleted carrier populations in the subthreshold regions. As electrons approach the resonant energies, their tendency to scatter by POP increases an order of magnitude and, if the broadening is large enough, they scatter before reaching E_{op}, thereby causing subthreshold valleys in $F(E)$. This effect is evident by comparing the distribution functions at 150 K with $\delta E_{ph}=1.6$ meV [Fig. 2(b)] to those at 300 K with $\delta E_{ph}=2.3$ meV [Fig. 2(a)]. The larger broadening at 300 K allows electron scattering well below the emission threshold, causing the depletion to extend to lower energies. In addition, POP absorption is more likely at 300 K, which gives rise to secondary minima such as those 18 meV above the first subband in Fig. 2(a). The peaks in the distribution functions just at E_{op} reflect POP absorptions from the bottom of the subband with a propagation of the peaking behavior to higher energies. Figure 3 demonstrates that at higher longitudinal fields, the electrons have more of a tendency to accelerate through the threshold regions without scattering, as evidenced by the relatively small subthreshold depopulation.

Another interesting feature of 1D distribution functions is the occurrence of intersubband population inversions under RISOPS conditions. This phenomenon has been explored in a previous paper[9] and found to have significant potential for far-infrared stimulated emission. Population inversion occurs for the second-order resonant configuration at 150 K [Fig. 2(b)] between the third

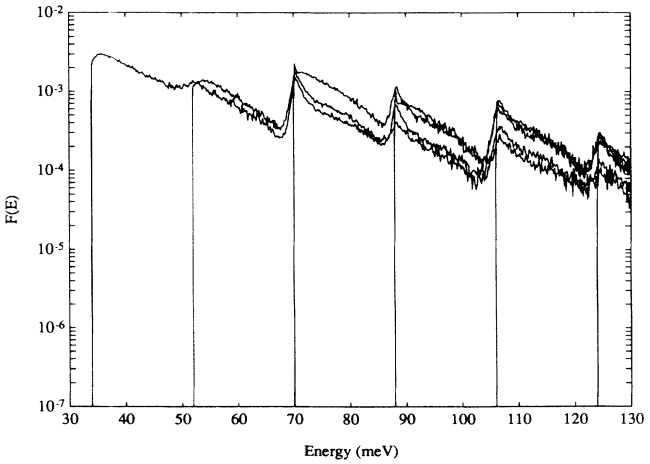

FIG. 3. Second-order resonant distribution functions with the same parameters as in Fig. 2 except with $F_x=200$ V/cm at 300 K.

(resonant) and second subbands with relative occupancies, O_{rel}, of 19.9% and 19.4%, respectively. The effect also shows up for the third-order configuration at 150 K (subband 4, $O_{rel}=14.0\%$; subband 3, $O_{rel}=11.8\%$). It should be noted that although population inversions exist between the harmonic-oscillator subbands discussed here, they tend to be weaker than those in systems with irregularly spaced subbands.[22] This is due to the propagation of the resonant intersubband coupling to the upper equally spaced subbands resulting from the harmonic-oscillator potential. This is particularly noticeable at room temperature, where population inversions do not occur because the higher absorption rate transfers electrons to the upper subbands more effectively, thereby smoothing out intersubband population anomalies. In addition, the potential for measuring stimulated emission between harmonic-oscillator subband should be reduced due to optical reabsorption.

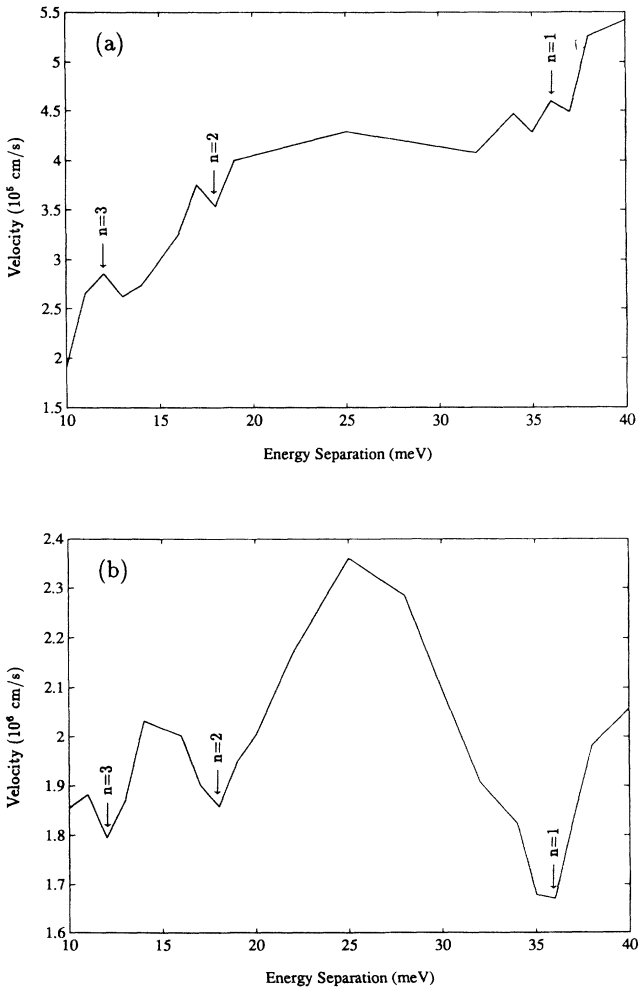

FIG. 4. Electron velocity as a function of subband energy separation at (a) $T=300$ K and (b) $T=150$ K. Both sets of data are taken for a system with $L_y=150$ Å and $F_x=50$ V/cm. The arrows indicate the position of high-order RISOPS (i.e., $n\Delta E=\hbar\omega_{LO}$).

The behavior of electron velocity with transverse harmonic-oscillator confinement is shown in Fig. 4. Note that the general increase in carrier velocities for both temperatures is consistent with the trend predicted by Sakaki[23] since, as the intersubband energy separation increases, upper subbands become excluded from the scattering processes and a general increase in carrier velocity with confinement is observed. Although *intra*subband scattering rates tend to increase with confinement,[8] their effect on carrier velocities in the regime of Fig. 4 is offset by the reduction of intersubband POP scattering.

The predominant features of Fig. 4 are the velocity fluctuations at resonant intersubband energy separations. These fluctuations, in the form of velocity minima, are a result of the strong coupling of the POP scattering mechanism to peaks in the 1D density of states (DOS). They are somewhat analogous to LMP oscillations of the longitudinal resistance observed in magnetically confined systems. The explanation of this phenomenon for magnetically confined systems depends on a nonmonotonic scattering rate and the dominance of the optical-phonon interaction over other mechanisms, both of which occur for electrostatically confined quasi-1D systems in GaAs. At resonance, intersubband POP scattering is dominated by transitions between subband minima.[10] Since both the initial and final states in these processes correspond to peaks in the 1D density of states, a significant increase in the overall POP scattering rate occurs and gives rise to a velocity minimum at resonance. Configurations above and below resonance generally have lower scattering rates due to the absence of the strong peak-to-peak intersubband transitions. This effect has been examined previously[22] for an electrostatically confined two-band model that demonstrated the decrease of average kinetic energy in the lower band and the subsequent increase in average kinetic energy of the upper band when the confinement is passed through resonance. The system considered here is just a generalization of the two-band model and can be expected to behave in a similar manner. Figure 4(a) shows that this oscillatory behavior is significantly less pronounced at room temperature than at 150 K [Fig. 4(b)]. The explanation is due to the larger DOS broadening at 300 K, which produces a smaller relative increase in the scattering rates under RISOPS conditions. Several interesting features of Fig. 4(a) are the split velocity minima near the first-order resonant configuration and the shift of the velocity minimum to a higher confinement energy for the third-order resonant configuration. A similar peak splitting was found in the transverse magnetoresistance by Warmenbol *et al.*,[24] who attribute it to the separate contributions of LO emission and absorption to ρ_{xx} in systems with relatively small broadening and low longitudinal fields. However, we believe that shift of the velocity minimum for the third-order configuration is due to poor resolution between resonant and near-resonant confinements, which is caused by the large broadening at room temperature coupled with the proximity between subbands ($\hbar\omega=12$ meV). For this reason we omit data for resonant configurations higher than third order.

CONCLUSION

With the aid of Monte Carlo simulation, we have demonstrated the emergence of intersubband dissipative transport in quasi-1D systems and generalized RISOPS to high orders. For parabolic confining potentials, velocity fluctuations and intersubband population inversions were shown to be quite prevalent at 150 K and significantly reduced, yet still observable, at room temperature. Such phenomena are attributed to the strong coupling between resonant subbands and other features unique to dissipative transport in parabolically confined quantized systems. Generally, these effects can be externally controlled via modulation of the confining potentials, which points to their application in semiconductor devices with nonlinear transport and optical characteristics.

ACKNOWLEDGMENTS

This work was supported by the Joint Services Electronics Program under Grant No. N00014-90-J-1270. All of the computations were performed using the resources of the National Center for Computational Electronics (NCCE) and the National Center for Supercomputing Applications (NCSA) at the University of Illinois.

[1]P. Petroff, A. Gossard, R. Logan, and W. Wiegmann, Appl. Phys. Lett. **41**, 635 (1982).
[2]T. Hiramoto, K. Hirakawa, Y. Iye, and T. Ikoma, Appl. Phys. Lett. **51**, 1620 (1987).
[3]M. Roukes, A. Scherer, S. Allen, H. Craighead, R. Ruthen, E. Beebe, and J. Harbison, Phys. Rev. Lett. **59**, 3011 (1987).
[4]E. Colas, E. Kapon, S. Simhony, H. Cox, R. Bhat, K. Kash, and P. Lin, Appl. Phys. Lett. **55**, 867 (1989).
[5]K. Ismail, D. Antoniadis, and H. Smith, Appl. Phys. Lett. **54**, 1130 (1989).
[6]S. Datta and M. McLennan, in *Nanostructure Physics and Fabrication*, edited by M. Reed and W. Kirk (Academic, Boston, 1989).
[7]T. Yamada and J. Sone, Phys. Rev. B **40**, 6265 (1989).
[8]S. Briggs and J. P. Leburton, Phys. Rev. B **38**, 8163 (1988).
[9]S. Briggs, D. Jovanovic, and J. P. Leburton, Appl. Phys. Lett. **54**, 2012 (1989).
[10]S. Briggs and J. P. Leburton, Superlatt. Microstruct. **5**, 145 (1989).
[11]V. Arora, Phys. Rev. B **23**, 5611 (1981).
[12]S. Briggs and J. P. Leburton, unpublished.
[13]H. Stormer, A. Gossard, and W. Wiegemann, Appl. Phys. Lett. **39**, 912 (1981).
[14]G. Fishman, Phys. Rev. B **36**, 7448 (1987).
[15]H. Fröhlich, H. Pelzer, and S. Zienau, Philos. Mag. **41**, 221 (1950).
[16]M. Stroscio, Phys. Rev. B **40**, 6428 (1989).
[17]K. Kim, B. Mason, and K. Hess, Phys. Rev. B **36**, 6547 (1987).
[18]S. Briggs, B. Mason, and J. P. Leburton, Phys. Rev. B **40**, 12 001 (1989).
[19]C. Jacoboni and L. Reggiani, Rev. Mod. Phys. **55**, 645 (1983).
[20]V. Gurevich and Y. Firsov, Zh. Eksp. Teor. Fiz. **47**, 734 (1964)[Sov. Phys.—JETP **20**, 489 (1965)].
[21]P. Vasilopoulos, P. Warmenbol, F. Peeters, and J. Devreese, Phys. Rev. B **40**, 1810 (1989).
[22]S. Briggs, D. Jovanovic, and J. P. Leburton, Solid State Electron. **32**, 12 (1989); **32**, 1657 (1989).
[23]H. Sakaki, Jpn. J. Appl. Phys. **19**, L735 (1980).
[24]P. Warmenbol, F. Peeters, and J. Devreese, Solid State Electron. **32**, 12 (1989); **32**, 1545 (1989).